

Response of a dipolar BEC to Laguerre–Gaussian beam driven STIRAP

Deepu Singh^{1, *}, Hari Sadhan Ghosh¹, Arpana Saboo¹, Soumyadeep Halder², and Sonjoy Majumder^{1, †}

¹*Department of Physics, Indian Institute of Technology Kharagpur, Kharagpur, West Bengal 721302, India*

²*Department of Physics, Indian Institute of Technology Gandhinagar, Gujrat 721302, India*

Coherent light–matter coupling via STIRAP can offer a versatile route to nucleate quantized vortices in Bose–Einstein condensates, yet its efficacy in dipolar condensates remains an open question. Can the orbital angular momentum of a Laguerre–Gaussian beam be coherently transferred to a dipolar BEC via STIRAP? We investigate this for a quasi-two-dimensional trapped dipolar condensate using co-propagating Gaussian and Laguerre–Gaussian laser beams. The interplay between long-range dipole–dipole interactions and short-range contact interactions enables access to three interaction-driven phases: superfluid, droplet, and supersolid. We find that the amount of angular momentum transferred from the optical field to the dipolar condensate, along with the nucleation and persistence of vortices, depends strongly on the underlying phases of the dipolar BEC. In the superfluid, STIRAP achieves near-complete population transfer and nucleates a stable, long-lived quantized vortex. In the droplet phase, although the vortex remains pinned within the density profile, the angular momentum is partially retained and oscillatory, accompanied by droplet fragmentation and recombination. In the supersolid phase, when the external magnetic field is oriented perpendicular to the LG beam’s propagation direction, the emergence of a modulated density distribution along with a slight reduction in inter-droplet coherence leads to vortex delocalization and eventually expels it along the field direction, yielding a vanishing average angular momentum. However, reorienting the magnetic polarization along the beam propagation direction restores efficient angular momentum transfer and stabilizes the vortex within the supersolid phase. Throughout the dynamics, collective modes, such as scissors and quadrupoles, emerge as phase-sensitive signatures of symmetry breaking and are affected by condensate rigidity. Overall, our results demonstrate a versatile route to engineer vortex states and probe collective excitations in dipolar Bose gases via coherent light–matter coupling.

I. INTRODUCTION

Coherent manipulation of quantum states in ultracold atomic systems can be achieved using the stimulated Raman adiabatic passage (STIRAP) technique [1–3], which enables nearly lossless population transfer between different internal or motional states through adiabatic evolution. In Bose–Einstein condensates (BECs), STIRAP has emerged as an efficient tool for coherent-state engineering, such as angular momentum transfer [4–7], and the generation of quantized vortices. Quantized vortices are a defining property of superfluids and have been extensively studied in Bose–Einstein condensates with purely short-range contact interactions [8–12]. In contrast, ultracold atomic gas with strong long-range anisotropic dipole–dipole interactions (DDI) [13, 14] produces vortices in a region of qualitatively different parameters in which the properties of the vortex are significantly modified. Since the DDI are both non-local and direction-dependent, they alter the structure of vortex cores and the dynamics of rotating condensates, such as critical rotation frequencies, distinct vortex-lattice geometries, and unconventional phase patterns compared to BECs [15, 16] with pure contact interaction. The Lee–Huang–Yang (LHY) correction [13, 17–19] considers quantum fluctuation in the system beyond the mean-field

theory and stabilizes the condensate to the new phases such as supersolids and self-bound droplets [20–25] under certain parameters. In literature, theoretical works supported by experiments agree that dipolar supersolids and droplets can foster vortices with anisotropic cores, and their behavior is linked to the underlying density modulations [19, 20, 26, 27]. In practice, vortex nucleation and elongated or distorted core structures have been generated in dipolar gases, such as quasi-2D Dysprosium (Dy) or Erbium (Er) condensates, using trap rotations [28–31], stirring a blue detuned laser beam [32], phase imprinting [33], or internal state coupling [34, 35]. In the supersolid region, both theoretical and experimental works indicate that vortices tend to reside in the superfluid regions between droplets, and their circulation patterns distinctively different from those of uniform superfluids.

One of the efficient processes for generating vortices in ultracold gases is through the orbital angular momentum (OAM) transfer from vortex light [4–7]. For instance, the OAM of Laguerre–Gaussian (LG) laser beams is $l\hbar$ per photon, where l is the integer winding number of the phase of light and plays a role in the internal and external motions of the atomic and molecular systems [36–38]. Such beams have been extensively employed to manipulate properties of matter, such as ultra-cold gases [39–46], enabling Raman-assisted spin-orbit coupling [3, 5, 47–50]. In the latter scheme, coherent Raman coupling is established between a vortex state of light and a non-rotating condensate, allowing for near-complete atom-population transfer into the vortex mode under suitable conditions.

* deepu.sy9880@gmail.com

† sonjoym@phy.iitkgp.ac.in

Recent experimental advancements in creating and stabilizing long-lived spin mixtures of ultracold dipolar Bose gas are feasible by suppressing dipolar relaxation and carefully tuning the short-range atom-atom interaction [51]. These advances now make it possible to apply this coherent state-engineering approach to dipolar systems, providing an ideal platform to explore the simultaneous roles of optical OAM transfer and intercomponent interactions in the dipolar regime [16, 52]. In particular, it enables the controlled creation of a vortex-carrying component within a dipolar Bose mixture, allowing us to investigate vortex-hosting superfluid, supersolid, and droplet configurations during Raman population transfer.

In this work, we examine the transfer of optical OAM to a dipolar Bose gas and study the associated population dynamics from non-rotating dBECs to Raman-coupled rotating dBECs with the help of a STIRAP [1–3] driven by a Laguerre-Gaussian pulse as a Stokes beam and a Gaussian pulse as a pump beam, and vice versa. We focus on investigating how the interaction-driven phases of a dipolar Bose gas, including the superfluid, supersolid, and droplet phases, influence the OAM transfer and the population transfer between different hyperfine states. To stabilize these phases against collapse, we derive the quasi-two-dimensional (quasi-2D) LHY correction for a binary dipolar mixture, enabling us to access supersolid and droplet configurations within our theoretical framework.

The remainder of this paper is organized as follows. In Sec. II, we outline the theoretical model for the OAM transfer mechanism in a dipolar BEC. In Sec. III describes the numerical methods used. In Sec. IV, we show that the interaction-driven phases (superfluid, supersolid, and droplet phase) of the dipolar Bose gas influence how the OAM is transferred, and whether efficient OAM is possible across these distinct phases. We further present our results on nearly complete population transfer, showing how interparticle interactions and Raman coupling determine the final population of the non-rotating component after transfer. In Sec. V, we summarize our findings and draw important conclusions. Appendix A presents the derivation of the underlying equations of motion from the system Hamiltonian, Appendix B details the derivation of the Lee-Huang-Yang (LHY) correction, and Appendix C discusses collective excitations such as scissors and quadrupole modes.

II. THEORY

We study the OAM transfer mechanism and its consequence from co-propagating Laguerre–Gaussian (LG) and Gaussian (G) beams to a quasi-2D dipolar BEC, tightly confined along z -axis as schematically shown in Fig. 1. Initially, the condensate is prepared in the non-rotating ground hyperfine state $|1\rangle$. The state $|3\rangle$ serves as an intermediate, electronically excited to a level far from resonance with large detuned frequency δ . $|2\rangle$ de-

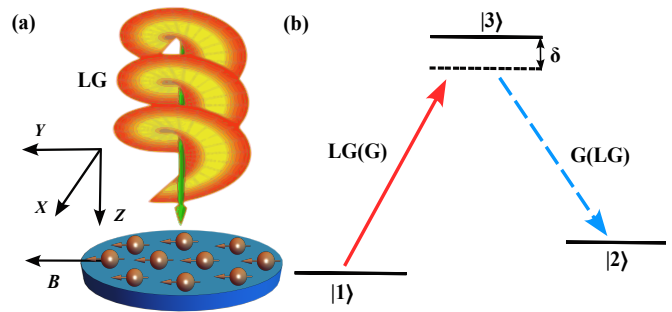


FIG. 1. (a) Schematic of a Laguerre-Gaussian (LG) beam propagating along the z -axis and interacting with a dipolar Bose-Einstein condensate (dBEC) confined in the x - y plane. The dipole moments are aligned by an external magnetic field applied along the y -direction. (b) Schematic of the electronic states considered, in a lambda (Λ) configuration. Specifically, the states of interest are $|1\rangle$ and $|2\rangle$, which represent the states associated with the two-component dipolar Bose-Einstein condensate (dBEC). $|8, -8\rangle$ is $|1\rangle$ and $|8, -7\rangle$ is $|2\rangle$ [51]. These two states are coupled, via $|3\rangle$, through detuned Gaussian (G) and Laguerre-Gaussian (LG) laser pulses. In this work, two laser pulse sequences are considered: (i) G-LG, where the Gaussian is the pump ($|1\rangle \rightarrow |3\rangle$) beam and the Laguerre-Gaussian is the Stokes ($|3\rangle \rightarrow |2\rangle$) beam, and (ii) LG-G, where the Laguerre-Gaussian is the pump ($|1\rangle \rightarrow |3\rangle$) beam and the Gaussian is the Stokes ($|3\rangle \rightarrow |2\rangle$) beam [6].

notes the final hyperfine state of the transition. There will be two physical situations depending on the choice of the pump and Stokes beam, which can be selected either as LG or G beams. If the pump beam carries OAM $l_1\hbar$ to excite the $|1\rangle \rightarrow |3\rangle$ transition and the Stokes beam with OAM $l_2\hbar$ drives the $|3\rangle \rightarrow |2\rangle$ transition, the state $|2\rangle$ acquires angular momentum $(l_1 - l_2)\hbar$. Although the dipole coupling between the $|1\rangle$ and $|2\rangle$ states is mediated through the intermediate state $|3\rangle$, the large detuning δ ensures that $|3\rangle$ remains essentially unoccupied throughout evolution. Hence, adiabatic elimination is allowed here. Under these conditions, coherent population transfer from $|1\rangle$ to $|2\rangle$ occurs.

The electric fields of the pump and Stokes beams can be expressed as

$$\mathbf{E}_j(\mathbf{r}, t) = \hat{\mathbf{e}}_j \mathcal{E}_j(t) r_{\perp}^{|l_j|} \exp\{-r_{\perp}^2/w_j^2\} \times \exp\{-i(k_j z - l_j \varphi - \omega_j t)\}, \quad (1)$$

where $\hat{\mathbf{e}}_j$, $\mathcal{E}_j(t)$, k_j , and ω_j denote the unit polarization vector, time-dependent amplitude, wave number, and frequency of the j -th pulse, respectively, with $j = 1, 2$ denoting the pump and Stokes fields. The radial coordinate in the transverse plane is given by $r_{\perp} = \sqrt{x^2 + y^2}$, w_j represents the beam waist, and φ denotes the azimuthal angle.

The temporal envelopes of the pulses are taken to be

Gaussian in the form

$$\mathcal{E}_j(t) = E_{\max} \exp\left\{-\frac{(t - \tau_j)^2}{T^2}\right\}, \quad (2)$$

where E_{\max} is the peak amplitude, τ_j is the temporal position of the pulse-centre, and T is the pulse duration [6, 53].

During coherent population transfer, the condensate will become a mixture of the same species but different hyperfine levels (two-component BEC). The coherent dynamics of the condensate components in the hyperfine states $|1\rangle$ and $|2\rangle$ under the STIRAP protocol are described by the macroscopic wave functions $\Psi_1(\mathbf{r}_\perp, t)$ and $\Psi_2(\mathbf{r}_\perp, t)$, respectively. Their temporal evolution follows a set of Raman-coupled extended Gross-Pitaevskii equations (eGPE) of the following form

$$\begin{aligned} i\hbar\partial_t\Psi_i(\mathbf{r}_\perp, t) = & \left[-\frac{\hbar^2}{2m_i}\nabla_\perp^2 + V_i^{\text{eff}}(\mathbf{r}_\perp) + (\Delta\mu_i)_{2\text{D}}^{\text{LHY}} \right. \\ & \left. + \sum_{j=1}^2 \left(G_{ij}|\Psi_j(\mathbf{r}_\perp, t)|^2 + c_{\text{dd}}^{ij}\mathcal{F}_{2\text{D}}^{-1}\{\tilde{n}_j(\mathbf{k}_\perp, t)F(\mathbf{k}_\perp l_z/\sqrt{2})\} \right) \right] \\ & \times \Psi_i(\mathbf{r}_\perp, t) + \mathcal{V}'(\mathbf{r}_\perp, t)\Psi_{3-i}(\mathbf{r}_\perp, t)e^{(-1)^i i(l_1 - l_2)\varphi}, \quad (3) \end{aligned}$$

where $i = 1, 2$. Here, light fields generate an additional spatial potential, leading to an effective potential for atoms in the i -th component as

$$V_i^{\text{eff}}(\mathbf{r}_\perp) = V_i(\mathbf{r}_\perp) + \mathcal{V}_i(t)r_\perp^{2|l_i|}e^{-2r_\perp^2/w_i^2}, \quad (4)$$

where $V_i(\mathbf{r}_\perp) = \frac{1}{2}m_i\omega^2(x^2 + \kappa^2 y^2)$ is the asymmetric 2D harmonic trapping potential with κ as the trap anisotropy parameter. Here, since we consider the same species in different hyperfine levels, mass of the atom $m_1 = m_2 = m$. The corresponding harmonic oscillator lengths are $l = \sqrt{\hbar/m\omega}$ and $l_z = \sqrt{\hbar/m\omega_z}$ for the radial and axial directions, respectively. The spatially dependent Raman coupling strength is given by $\mathcal{V}'(\mathbf{r}_\perp, t) = \sqrt{\mathcal{V}_1(t)\mathcal{V}_2(t)}(r_\perp)^{(|l_1|+|l_2|)}e^{-(r_\perp^2)(1/w_1^2+1/w_2^2)}$, where $\mathcal{V}_i(t) = \mathcal{V}_{\max}e^{-2[(t-\tau_i)/T]^2}$ and $\mathcal{V}_{\max} = E_{\max}^2 d^2/\hbar\delta$ and d is the induced electric dipole moment.

The coupling constant $G_{ij} = 2\sqrt{2\pi}\lambda a_{ij}\hbar^2/ml$ in Eq. 3 represents the short-range intra- ($i = j$) and inter-species ($i \neq j$) contact interaction strengths, where $\lambda = \omega_z/\omega$ is the trap aspect ratio with ω_z as trap frequency along z -direction and a_{ij} is the s -wave scattering length. The dipole-dipole interaction is calculated first in the Fourier domain and transferred back to the real space using the inverse Fourier transformation in the quasi-2D frame, and obtained $\mathcal{F}_{2\text{D}}^{-1}$. The function $F(\mathbf{q})$ represents the DDI in momentum space for a quasi-2D geometry [54–60] with its coupling strength $c_{\text{dd}}^{ij} = \mu_0\mu_i^m\mu_j^m/(3\sqrt{2\pi}l_z)$, where μ_0 is the vacuum permeability and μ_i^m ($i = 1, 2$) is the magnetic moment, and $\mathbf{q} = \mathbf{k}_\perp l_z/\sqrt{2}$. $F(\mathbf{q}) = \cos^2(\alpha)F_\perp(\mathbf{q}) + \sin^2(\alpha)F_\parallel(\mathbf{q})$,

where α is the angle between the polarization unit vector $\hat{\mathbf{d}}$ and the z -axis, $F_\perp(\mathbf{q}) = 2 - 3\sqrt{\pi}qe^{q^2}\text{erfc}(q)$, and $F_\parallel(\mathbf{q}) = -1 + 3\sqrt{\pi}\frac{q_d}{q}e^{q^2}\text{erfc}(q)$, where \mathbf{q}_d is the wave vector along the direction of the projection of $\hat{\mathbf{d}}$ onto the x - y plane, and erfc representing the complementary error function. Here, $\tilde{n}_j(\mathbf{k}_\perp, t)$ is the 2D Fourier transformation of density $n_j(\mathbf{r}_\perp, t)$.

In this work, we investigate the impact of the STIRAP protocol on dipolar BEC phases, including the dominant dipole-dipole interaction-driven density modulated phases, such as the droplet and supersolid phases. The mean-field theory fails to explain the stability of these phases against collapse, compelling the LHY correction crucial for the realization of stable droplets and supersolids. The third term in Eq. (3) accounts for the correction in the chemical potential due to the quantum fluctuations (known as LHY correction), derived in Appendix B for the quasi-2D case, is expressed as

$$(\Delta\mu_i)_{2\text{D}}^{\text{LHY}} = \frac{m^{3/2}\lambda^{3/4}}{3\sqrt{5}\pi^2\hbar^3 l^{3/2}\pi^{3/4}} \sum_{\pm} \int_0^\infty du \text{Re}(I'_{E\pm}), \quad (5)$$

where

$$\begin{aligned} I'_{E\pm} = & \left(\tilde{V}_{ii}^{\text{int}}(u) \pm \frac{(-1)^{i-1}\delta\tilde{V}_{ii}^{\text{int}}(u) + 2\tilde{V}_{12}^{\text{int}}(u)^2 n_{3-i}}{\sqrt{\delta^2 + 4\tilde{V}_{12}^{\text{int}}(u)^2 n_1 n_2}} \right) \\ & \times \left(n_1 \tilde{V}_{11}^{\text{int}}(u) + n_2 \tilde{V}_{22}^{\text{int}}(u) \pm \sqrt{\delta^2 + 4\tilde{V}_{12}^{\text{int}}(u)^2 n_1 n_2} \right)^{3/2}. \quad (6) \end{aligned}$$

$\delta = n_1 \tilde{V}_{11}^{\text{int}}(u) - n_2 \tilde{V}_{22}^{\text{int}}(u)$, $\tilde{V}_{ij}^{\text{int}}(u) = \tilde{g}_{ij}^c + \tilde{V}_{\text{dd}}^{ij}(u)$, being the 2D Fourier transform of the total interaction potential.

Initially, in the absence of the optical fields of lasers, all atoms are assumed to occupy the lowest hyperfine state $|1\rangle$ and form a condensate. Upon interaction with the optical fields, the atoms are coherently transferred from state $|1\rangle$ to $|2\rangle$ via a STIRAP as described in Eq. (3). At any instant of time, during the population transfer total number of atoms are conserved, i.e., $\int (|\Psi_1|^2 + |\Psi_2|^2) d\mathbf{r}_\perp = N_1 + N_2 = N$, where N_1 and N_2 denote the number of atoms in components $|1\rangle$ and $|2\rangle$, respectively.

The transferred atoms acquire an orbital angular momentum of $(l_1 - l_2)\hbar$, represented as a phase factor $e^{i(l_1 - l_2)\varphi}$ in the wavefunction Ψ_2 . The presence of this phase factor in Eq. (3) prevents the transfer of the population back from the hyperfine state $|2\rangle$ to the state $|1\rangle$. This transfer of OAM from light to the condensate Ψ_2 results in the nucleation of quantized vortices. Due to the single-valuedness of the condensate wavefunction, the phase must satisfy the quantization condition of an integer multiple of 2π , characterized by a phase winding of $\mathcal{L}_q \times 2\pi$, where $\mathcal{L}_q = l_1 - l_2$ denotes the vortex topological charge.

III. NUMERICAL METHODS

In this work, following the STIRAP protocol, the dynamics is governed by numerical simulations of the set of Raman-coupled eGPE (3). For the sake of convenience of numerical simulations and better computational precision, we cast Eq. (3) into a dimensionless form. This is achieved by rescaling the length scale and time scale in terms of oscillator length l and trapping frequency ω . Under this transformation, the wave function of the condensate in the hyperfine state $|i\rangle$ obeys $\Psi'_i(\mathbf{r}) = \sqrt{l^2/N_i}\Psi_i(\mathbf{r})$, where N_i is the number of particles in the state $|i\rangle$. After the transformation of variables into dimensionless quantities, the coupled eGPE (3) is solved by the split-step Crank-Nicolson scheme [61, 62].

First, the initial configuration of the ground state is obtained by propagating Eq. (3) in imaginary time until the relative deviation of the condensate wave function, Ψ_1 , between successive time steps becomes smaller than 10^{-6} , while Ψ_2 is considered zero. This solution is then used as the initial state for the dynamical simulations, where Eq. (3) is propagated in real time following the STIRAP protocol. The STIRAP process is implemented using a combination of G-LG or LG-G pulse sequences acting as the pump and Stokes beams. The widths of both pulses are fixed at $T = 4\omega^{-1}$, with $\tau_1 = 9.9\omega^{-1}$ and $\tau_2 = 1.4\omega^{-1}$. The LG beam has a waist $w = 15l$. Our simulations are performed within a 2D square grid containing (512×512) grid points with the spatial grid spacing $\Delta x = \Delta y = 0.08l$ while the time step $\Delta t = 2 \times 10^{-4}/\omega$.

IV. RESULTS AND DISCUSSION

In this work, we consider a dipolar BEC of ^{162}Dy atoms with the lowest two hyperfine states $|8, -8\rangle$ and $|8, -7\rangle$ defined as the initial $|1\rangle$ and final $|2\rangle$ states [51], respectively. The dipole moments corresponding to these hyperfine states are $-9.93 \mu_B$ and $-8.69 \mu_B$, respectively. Atoms with the $|8, -8\rangle \equiv |1\rangle$ state are prepared in the presence of an external magnetic field along the y -axis and subsequently investigated their response under the STIRAP protocol governed by Eq (3) with the sequence of LG and G pulses, as well as the corresponding G-LG configuration. The system consists of $N = 6 \times 10^4$ number of dipolar atoms confined in a circularly symmetric quasi-2D harmonic trap with a relatively smaller trapping frequency in the x - y plane $\omega = 2\pi \times 45$ Hz and the system experiences strong confinement along the z -direction, characterized by $\lambda = \omega_z/\omega = 20$ [55–60]. The quasi-2D condition, $\hbar\omega_z \gg \mu_{1(2)}$, is maintained throughout the process. The transfer of angular momentum and the dynamical evolution of the condensate are sensitive to both intra- and inter-species DDI as well as the contact-interaction strengths. A harmonically trapped dipolar BEC can exhibit superfluid (SF), supersolid (SS) and isolated droplet (ID) phases [20, 21, 23, 24, 28, 29] de-

pending on the relative strength of DDI over the contact interaction strength, which can be achieved experimentally [63–66].

A. Superfluid Phase

We first examine the impact of the STIRAP protocol on the SF phase. To obtain the SF phase at Ψ_1 and Ψ_2 , we choose relatively larger intra-species scattering lengths among atoms at both the hyperfine levels $|1\rangle$ and $|2\rangle$. Here, we consider $a_{11} = a_{22} = 140a_0$ compared to dipolar lengths $a_{11}^{\text{dd}} = 131a_0$, $a_{22}^{\text{dd}} = 100.3a_0$ and inter-species scattering length $a_{12} = a_{21} = 150a_0$. The coherent population transfer from $|1\rangle$ to $|2\rangle$ controlled by STIRAP pulse sequence on the initially prepared SF state, shown in Figs. 2(a1), with a Gaussian beam ($l_1=0$) and a Laguerre-Gaussian beam ($l_2=1$) as pump and Stokes beams, respectively, with peak amplitude $\nu_{\text{max}} = 100 \hbar\omega$. The Gaussian pump beam generates an effective repulsive potential around the center of Ψ_1 [see Eq. (4)]. It initiates a coherent transfer of atoms via a STIRAP primarily from the central region of Ψ_1 . As the system evolves over time, atoms are progressively depleted from state $|1\rangle$ and populate state $|2\rangle$. During population transfer, the system exhibits a mixture of transient immiscible superfluid phase, as seen in the density profiles in Figs. 2(a2-a3, b2-b3) in $t = 22.10$ ms. The spatial dependence of the coupling term in Eq. (3) enforces density depletion at the center ($r_{\perp} = 0$) of Ψ_2 , while the associated phase factor transfers angular momentum, leading to the formation of a vortex with topological charge $l_1 - l_2 = -1$ in the second component. The associated evolution of the angular momentum is shown in Fig. 2 (c). Its oscillatory evolution is justified from the study of the excited scissors and quadrupole modes during the population and angular momentum transfer dynamics (see Appendix C). As a result, the angular momentum of Ψ_2 exhibits fluctuations about $L_{z2}/N = -\hbar$, forming a characteristic beating pattern. The nearly complete population transfer from $|1\rangle$ to $|2\rangle$ is achieved by $t = 44.21$ ms, as shown in Figs. 2(a4, b4).

In contrast, when an LG-G pulse sequence is performed under the STIRAP process, the relatively small spatial overlap between the pump LG beam and Ψ_1 requires a higher peak amplitude, $\nu_{\text{max}} = 500 \hbar\omega$, in order to achieve 100% population transfer from $|1\rangle$ to $|2\rangle$. In this case, the annular intensity profile of the LG pump beam generates an effective repulsive potential at the periphery of Ψ_1 [see Eq. (4)], causing the transfer to initiate predominantly from the outer region of Ψ_1 to Ψ_2 as shown in Figs. 2(d2, d3). Similar to the previous case, the spatially dependent Raman coupling is weak near the center of the trap and stronger at the periphery, resulting in a population enrichment observed in the peripheral region of Ψ_2 [Fig. 2(e2)]. This density population combines with the phase factor $e^{-i(l_1-l_2)\varphi}$ in the coupling term of Eq. (3), leading to the nucleation of a vortex with topo-

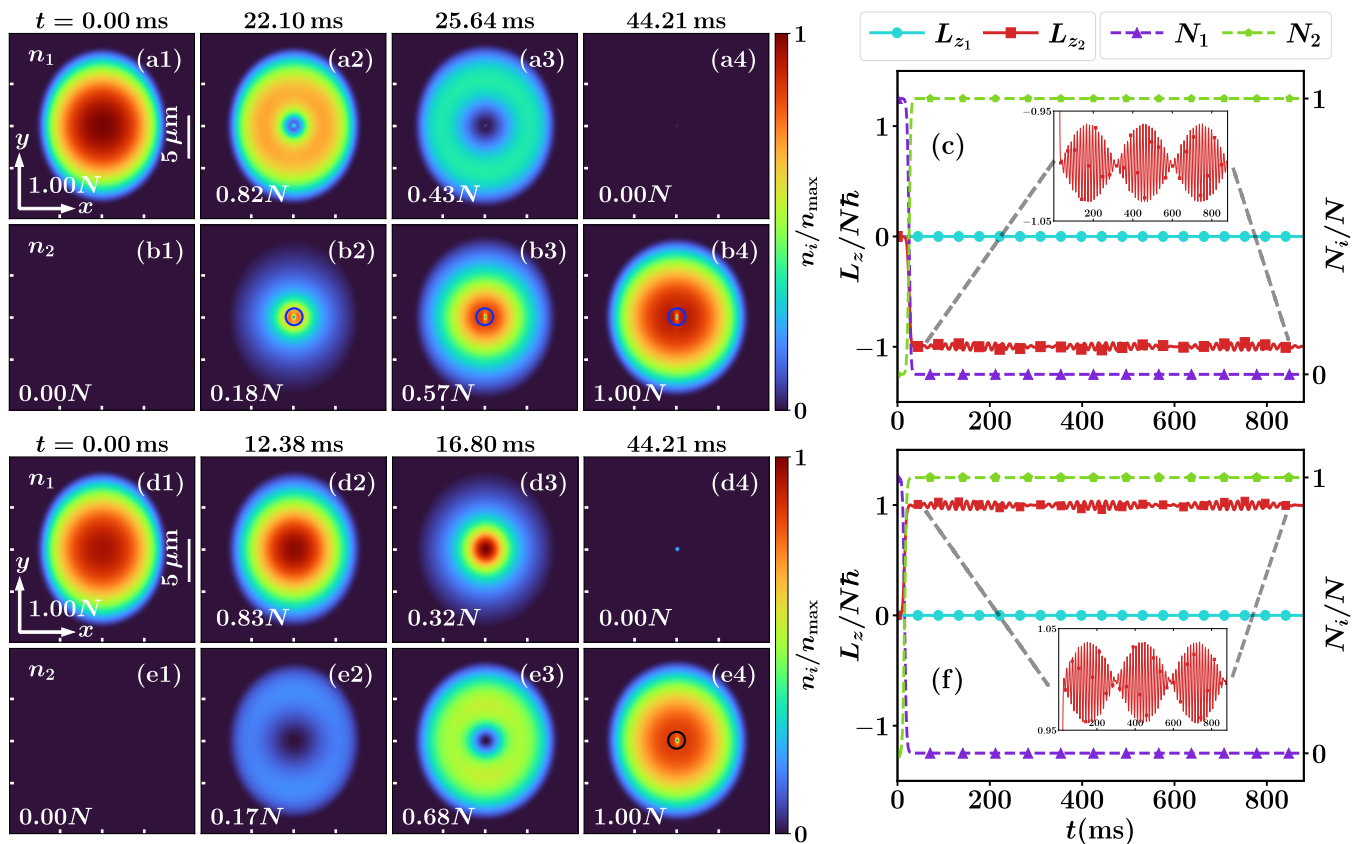


FIG. 2. Time-resolved density distributions of the condensate are displayed in panels (a1–a4) and (d1–d4) for atoms in state $|1\rangle$, and in panels (b1–b4) and (e1–e4) for atoms in state $|2\rangle$. In panels (b1–b4), a vortex of charge -1 is generated in Ψ_2 by LG beam, while (e1–e4) correspond to the case of a $+1$ vortex. During the evolution, the population of Ψ_2 increases steadily. In the -1 vortex (blue circle) case, atoms are initially transferred from Ψ_1 to Ψ_2 near the trap center, whereas for the $+1$ vortex (black circle) case, the transfer begins predominantly at the outer region of the trap. Time evolution of the angular momentum L_{z_i} and atom populations N_i in both states is shown in panel (c) for the G-LG pulse sequence and in panel (f) for the LG-G pulse sequence. Solid and dashed lines represent $L_{z_i}/(N\hbar)$ and N_i/N , respectively.

logical charge $l_1 - l_2 = +1$ [see Figs. 2(e3, e4)]. The transfer of angular momentum to Ψ_2 during the dynamics is illustrated in Fig. 2(f). Furthermore, similar to the G-LG sequence, the nonuniform, spatially dependent particle transfer, together with slight density deformation induced by the in-plane magnetic field, excites collective modes in Ψ_2 (see Appendix C) [67–75].

B. Droplet phase

So far, our study has focused on the transfer of particles and angular momentum within the weak DDI regime. In the strongly interacting DDI regime, dipolar BECs are known to support exotic self-bound and crystalline phases, including quantum droplets. To realize the single-droplet (SD) phase in the lowest hyperfine state $|1\rangle$, we consider a significantly smaller intra-species scattering length, $a_{11} = 70a_0$, relative to the corresponding dipolar length $a_{11}^{\text{dd}} = 131a_0$. For these parameters, and in the absence of pump and Stokes laser fields, the

dipolar condensate forms a self-bound droplet characterized by a negative chemical potential ($\mu < 0$) and an elongation along the y -axis, i.e., the direction of external polarization [see Figs. 3(a1) and 3(d1)]. To ensure that the system remains in the droplet phase following particle transfer from state $|1\rangle$ to $|2\rangle$, we consider $a_{22} = a_{11} = 70a_0$. We investigate the impact of STIRAP in the presence of weak short-range inter-species interactions. We consider weak inter-species coupling with $a_{12} = a_{21} = 73a_0$.

As the atoms are transferred, the droplet in Ψ_1 shrinks, as shown in Figs. 3(a1–a3 and d1–d3). However, the formation and property of the droplet in Ψ_2 differ qualitatively and quantitatively between the pulse sequences. For example, the G-LG pulse sequence with $\nu_{\text{max}} = 200\hbar\omega$ nucleates a new droplet in Ψ_2 around the center of the condensate mixture. Atoms away from the center rapidly convert to the state $|2\rangle$ and form a self-bound droplet, Ψ_2 , which hosts a quantized vortex with charge -1 (Figs. 3(b2–b3)). A notable feature of this droplet occurs when most of the atoms have undergone the transition to the state $|2\rangle$. The droplet at Ψ_2 frag-

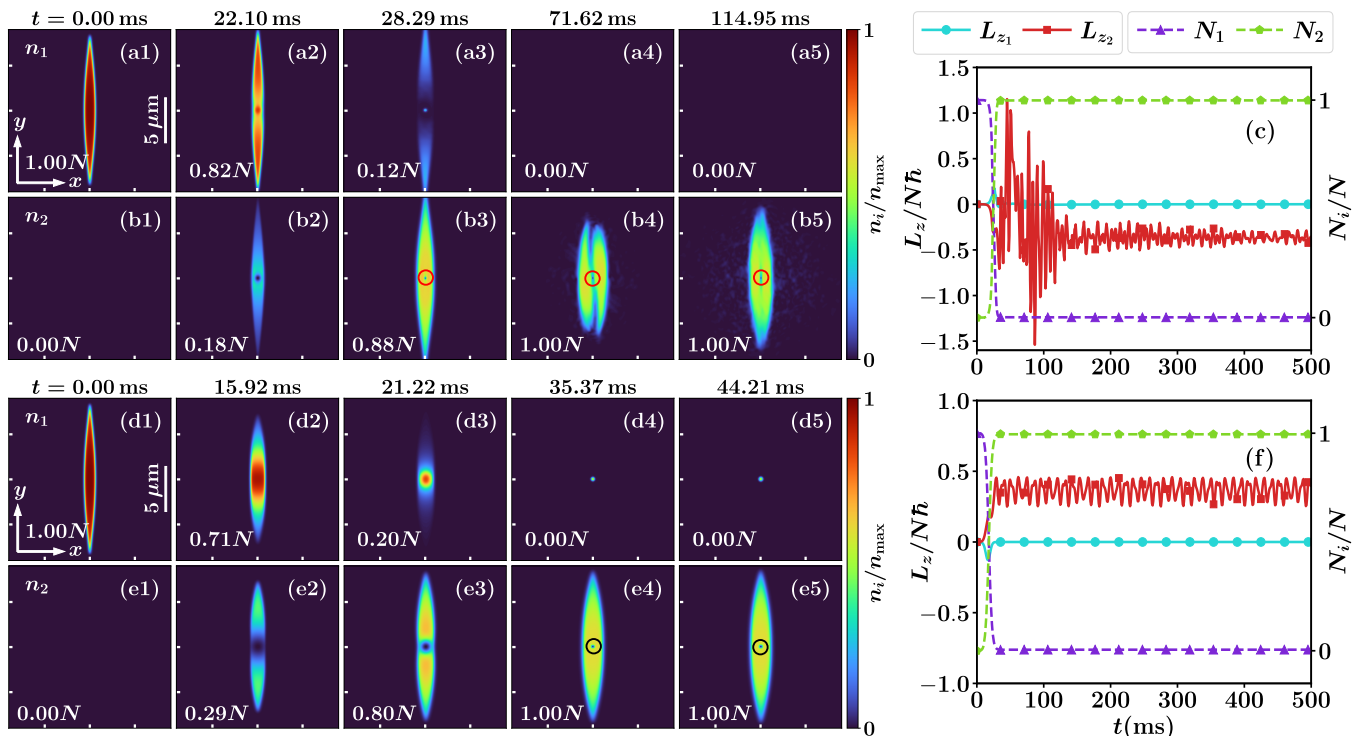


FIG. 3. Time-resolved density distributions of the condensate are displayed in panels (a1–a5) and (d1–d5) for atoms in state $|1\rangle$, and in panels (b1–b5) and (e1–e5) for atoms in state $|2\rangle$. In panels (b1–b5), a vortex of charge -1 is generated in Ψ_2 by LG beam, while (e1–e5) correspond to the case of a $+1$ vortex. During the evolution, the population of Ψ_2 increases steadily. In the -1 vortex (red circle) case, atoms are initially transferred from Ψ_1 to Ψ_2 near the trap center, whereas for the $+1$ vortex (black circle) case, the transfer begins predominantly at the outer region of the trap. Time evolution of the angular momentum L_{z_i} and atom populations N_i in both states is shown in panel (c) for the G-LG pulse sequence and in panel (f) for the LG-G pulse sequence. Solid and dashed lines represent $L_{z_i}/(N\hbar)$ and N_i/N , respectively.

ments into two droplets around $t \approx 39.79$ ms, which remain separated for a significant duration before merging starts at $t \approx 71.62$ ms, as shown in Figs. 3(b4). The merging reflects the preferred self-bound nature of the droplet, which energetically favors a single compact configuration [33]. Throughout this process, the vortex remains trapped within the droplet (Figs. 3(b5)), though its position varies compared to the center of mass of the condensate.

In contrast, for the LG-G pulse sequence, we consider $\nu_{\max} = 800\hbar\omega$ for the complete transfer of atoms from state $|1\rangle$ to $|2\rangle$ and the process starts from the periphery, as in the case of a superfluid. The vortex of quantized charge $+1$ is popped in the center of the droplet state Ψ_2 around $t \approx 21.22$ ms, when a large fraction of the atom population is transferred to the state $|2\rangle$ (See Figs. 3(d3–e3)).

The fragmentation of droplets in Ψ_2 is largely suppressed here, unlike the case of G-LG. As expected, a quantized vortex with charge $+1$ is formed (see Figs. 3(e3–e5)). Rather than splitting, the condensate remains intact as a single, compact droplet, retaining its vortex. Figs. 3(c, f) show that the angular momentum L_z oscillates with the non-zero mean value. The value of

L_z oscillates during the initial motion of the vortex for the G-LG pulse sequence. In this case, the damping of the oscillation at later times ($t > 100$ ms) is likely associated with the rigidity of the droplet states, an argument supported by the analysis of the scissors mode discussed in Appendix C.

Although the spatial effects of two pulse sequences on the dipolar condensate differ, the droplet phase of Ψ_2 exhibits a common qualitative feature. The transferred angular momentum is confined within a finite density peak and, therefore, is strongly coupled to its collective motion [68–71, 73]. Unlike the extended superfluid phases, the droplet cannot redistribute circulation through bulk flow. Instead, vortex dynamics become intertwined with global shape oscillations [76] and fragmentation processes. In the G-LG case, droplet splitting and subsequent merging allow a vortex. In contrast, for the LG-G sequence, the droplet remains largely intact, and the vortex persists without fragmentation-driven reconfiguration. The long-time oscillatory behavior of the angular momentum reflects the non-conservation of L_z (Figs. 3(c, f)) and scissor mode excitation. We further discuss the temporal evolution of the corresponding collective excitations in Appendix C for both the G-LG and LG-G pulse se-

quences.

In contrast to the quasi-2D droplet with magnetic-field polarization along the y -direction, where the transferred vortex remains stable within the condensate, the vortex in the z -polarized droplet configuration becomes dynamically unstable because the LG beam is aligned parallel to the dipole polarization direction. In this geometry, the vortex core removes a density tube dominated by attractive head-to-tail dipolar interactions, thereby inducing droplet splitting or vortex-line instability [77]. In contrast, the y -polarized droplet configuration predominantly removes repulsive dipolar regions, which stabilizes the vortex state.

C. Supersolid phase

In the supersolid regime, realized for $\kappa = 2.5$ with intra-species scattering lengths $a_{11} = 84a_0$ and $a_{22} = 72a_0$ and inter-species scattering length $a_{12} = a_{21} = 82a_0$, the ground-state solution of Eq. (3) corresponds to a supersolid configuration in state $|1\rangle$.

For the G-LG pulse sequence with $\nu_{\max} = 100\hbar\omega$, the response to injection of orbital angular momentum depends delicately on the spatial structure and strength of the Raman coupling. Atoms in the central region start to transfer first and we observe the depletion of the superfluid background atoms in $|1\rangle$ leading to the underlying density modulation and gives rise to elongated droplets, as shown in Figs. 4(a1-a3). Rather than preserving the original droplet symmetry, the supersolid in $|1\rangle$ becomes anisotropic during transfer dynamics. The density-modulated structure of Ψ_2 gradually develops together with a vortex of charge -1 around $t \approx 19.45$ ms, [see Figs. 4(b2)]. The density gap along the y -axis is due to the domination of density modulation along the x -axis with a very small superfluid fraction around $t \approx 42.44$ ms [see Figs. 4(b4)]. The newly formed supersolid state shows a breathing motion and stabilizes with time. The supersolid forms around $t \approx 88.3$ ms without a vortex.

Similarly to the SF and droplet cases, atom-transfer begins at the periphery of Ψ_1 for the LG-G beam sequence with $\nu_{\max} = 500\hbar\omega$, and the outer density modulation is first destabilized. As a result, the supersolid structure in Ψ_1 temporarily collapses to a more uniform density profile before re-establishing the modulation, as seen in Figs. 4(e2-e3). The intermediate configurations reveal a journey of superfluid-to-supersolid transitions rather than a simple droplet. In Ψ_2 , the supersolid develops from the edge toward the center and hosts a vortex with circulation $+1$ at around $t \approx 22.99$ ms [see Figs. 4(e3)]. Due to the breathing mode, the supersolid becomes elongated along the x -axis, while a weak connection develops along the y -direction between the droplets on both sides around ≈ 39.79 ms, as shown in Fig. 4(e4).

The early-time dynamics of the condensate for both pulse sequences exhibit a reduced population in the central region of Ψ_2 . Over longer times, the density of the

supersolid state, Ψ_2 , becomes a disconnected, two-lobed density-modulated structure, as shown in Figs. 4(b5-e5). Although the long-time configuration is qualitatively similar in both pulse sequences, the transient pathways differ substantially; elongated droplet formation dominates for G-LG, whereas transient suppression of density modulation precedes reorganization in the LG-G case. As expected, the angular momentum, $|L_z|$, initially approaches a unit value over a few milliseconds during which a vortex is formed. Then the angular momentum continues to oscillate around zero for a long time, indicating repeated π -phase jumps and loss of vortex from the condensate, as shown in Figs. 4(c, f). The oscillation of angular momentum and the resulting vortex dynamics are accompanied by the excitation of several collective modes of the condensate, discussed in the Appendix C.

We can understand the development of density modulation in the supersolid structure of condensate from the rotational (E_{IC}) and irrotational (E_C) parts of the kinetic energy [78, 79]. For this purpose, we use the density-weighted velocity field $\mathbf{u} = \frac{\hbar}{m}\sqrt{\rho}\nabla\phi$, where ρ and ϕ denote the condensate density and phase, respectively. The kinetic energy contributions are given by

$$E_C = \frac{m}{2} \int d\mathbf{r} |\mathbf{u}^C|^2,$$

$$E_{IC} = \frac{m}{2} \int d\mathbf{r} |\mathbf{u}^{IC}|^2,$$

where the compressible velocity field \mathbf{u}^C is curl-free, while the incompressible component \mathbf{u}^{IC} is divergence-free.

The compressible (E_C) and incompressible (E_{IC}) energies rise rapidly at the initial stage, as shown in Figs. 5(a) and (b), for both pulse sequences of G-LG and LG-G. During this stage, density modulations develop and phase gradients build up, marking the onset of the supersolid state. The peak in E_C reveals a significant rearrangement of density as the modulated structure forms, while the increase in E_{IC} suggests the temporary development of vortex in the region of low superfluid fraction around ≈ 89.3 ms to ≈ 93.72 ms for the G-LG case (see attached video). In the case of LG-G beam sequence, the two side lobes of the supersolid come close and go apart. This process forms a transient vortex, leading to a large oscillation of E_{IC} for ~ 60 ms.

Later, at $t \gtrsim 100$ ms), E_{IC} becomes close to zero, indicating loss of vortex. In contrast, the oscillation of E_C decays slowly, indicating persistent density modulation. It also suggests that part of the vortex energy is redistributed into phonon-like modes. This implies that the supersolid structure remains intact with its two lobes but without a sustained vortex. In a nutshell, the compressible and incompressible energy profiles, along with the density modulation, indicate that the vortex, which formed at an early stage of population transfer through light, eventually disappears in supersolid, unlike in superfluid or droplet cases, as discussed earlier.

In contrast to the quasi-2D supersolid with magnetic-field polarization along the y -axis, where the vortex

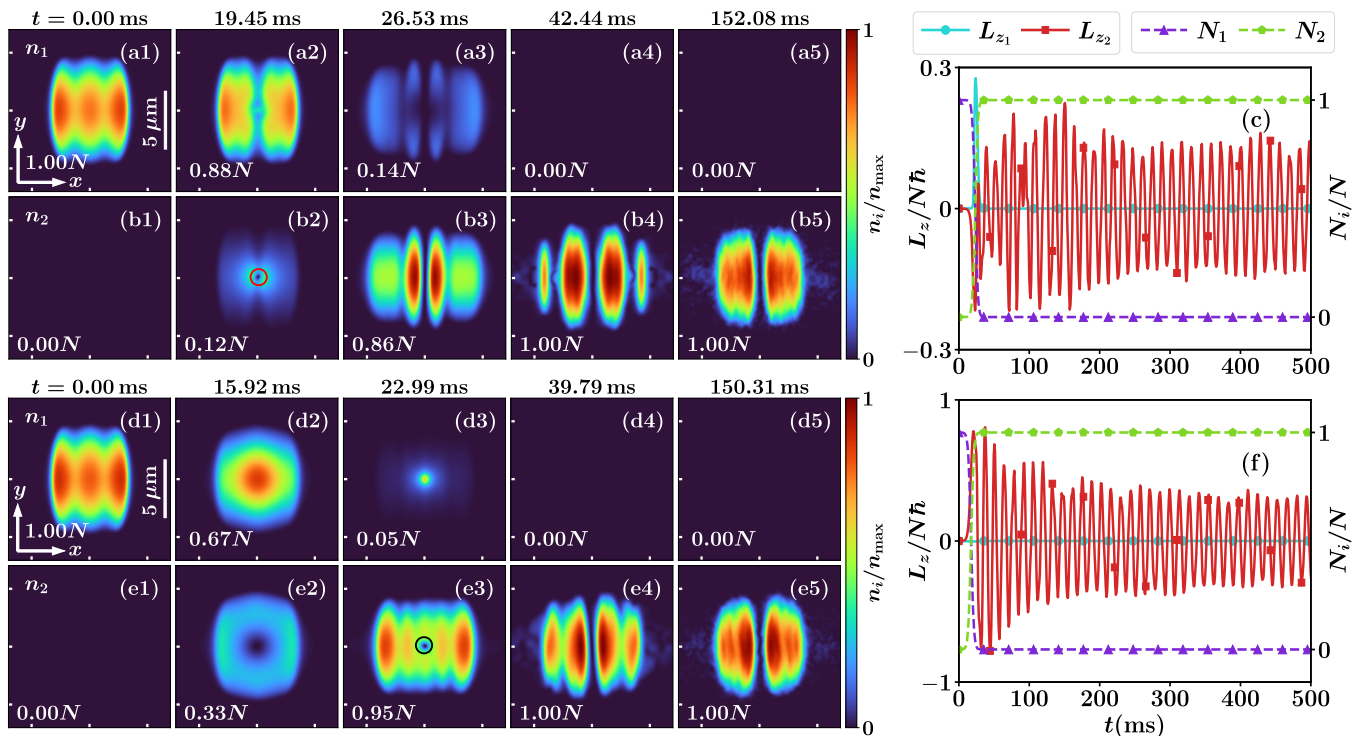


FIG. 4. Time-resolved density distributions of the condensate are displayed in panels (a1–a5) and (d1–d5) for atoms in state $|1\rangle$, and in panels (b1–b5) and (e1–e5) for atoms in state $|2\rangle$. In panels (b1–b5), a vortex of charge -1 is generated in Ψ_2 by LG beam, while (e1–e5) correspond to the case of a $+1$ vortex. During the evolution, the population of Ψ_2 increases steadily. In the -1 vortex (red circle) case, atoms are initially transferred from Ψ_1 to Ψ_2 near the trap center, whereas for the $+1$ vortex (black circle) case, the transfer begins predominantly at the outer region of the trap. Time evolution of the angular momentum L_{z_i} and atom populations N_i in both states is shown in panel (c) for the G-LG pulse sequence and in panel (f) for the LG-G pulse sequence. Solid and dashed lines represent $L_{z_i}/(N\hbar)$ and N_i/N , respectively.

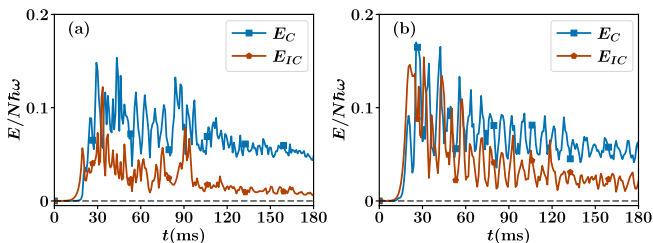


FIG. 5. Time evolution of the compressible energy E_C and incompressible energy E_{IC} for the supersolid phase for (a) the G-LG pulse sequence and (b) LG-G pulse sequence of state $|2\rangle$.

leaves the condensate, the supersolid with z -axis polarization exhibits long-lived vortex states. In this case, the vortex remains trapped within the condensate with topological charge -1 , while the transferred component simultaneously develops a well-defined density-modulated supersolid structure. The enhanced stability arises from the alignment of both the magnetic field polarization and the LG-beam propagation along the z -direction.

Effect of parallel alignment of the magnetic field and the beam propagation direction

When the external magnetic field is aligned parallel to the beam propagation direction, i.e., along the z -axis, the trap aspect ratio λ must be reduced to enhance the attractive DDI and realize the initial supersolid state. In this configuration, the supersolid state in state $|1\rangle$ is realized for $\lambda = 2.95$, $\kappa = 1$, and $N = 10^5$, with intra-species scattering lengths $a_{11} = 91a_0$ and $a_{22} = 71a_0$, and inter-species scattering lengths $a_{12} = a_{21} = 90a_0$. Due to the relatively small value of λ , the quasi-2D approximation is no longer valid in this regime. Consequently, we solve Eq. (A2) using the full three-dimensional numerical approach within the beyond-mean-field framework.

For the G-LG pulse sequence with $\nu_{\max} = 200\hbar\omega$, atoms are transferred from the central region of the supersolid in state $|1\rangle$ to state $|2\rangle$. As the transfer starts, density-modulated droplets remain in $|1\rangle$ while gradually emerging in $|2\rangle$ at around ≈ 18.57 ms [see Figs. 6(a2-b2)]. At intermediate times [see Figs. 6(a3-b3)], both states $|1\rangle$ and $|2\rangle$ contain modulated superfluid background at around ≈ 24.76 ms. With increasing population transfer, this background gradually evolves into a well-defined su-

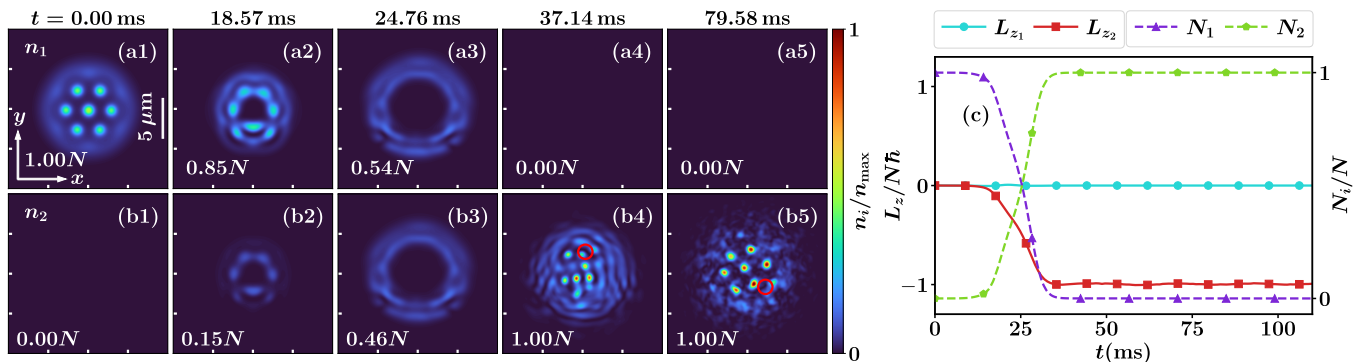


FIG. 6. Time-resolved density distributions of the z -aligned supersolid condensate are shown in panels (a1–a5) for atoms in state $|1\rangle$ and in panels (b1–b5) for atoms in state $|2\rangle$. In panels (b1–b5), a vortex (red circle) with topological charge -1 is generated in Ψ_2 by the LG beam. During the evolution, the population of Ψ_2 increases steadily. Time evolution of the angular momentum L_{z_i} and atom populations N_i in both states is shown in panel (c) for the G-LG pulse sequence. Solid and dashed lines represent $L_{z_i}/(N\hbar)$ and N_i/N , respectively.

persolid structure [see Fig. 6(b4)] at around ≈ 37.14 ms. At the same time, a quantized vortex with topological charge -1 is created in $|2\rangle$ through the orbital angular momentum carried by the LG beam [see Fig. 6(b4–b5)].

During the transfer [see Figs. 6(b2–b3 and b5)], the size of the supersolid in state $|2\rangle$ grows from the center toward the outer region and finally becomes a complete supersolid. The vortex with charge -1 remains trapped inside the supersolid, as light-matter coupling weakens. The angular momentum remains nearly constant for more than 100 ms, as shown in Fig. 6(c). Since the angular momentum L_z commutes with the Hamiltonian because the magnetic field and the LG beam propagation direction are the same, the transferred angular momentum is conserved. As a result, no noticeable collective excitation is observed during the evolution.

Similar behavior is observed for the LG-G pulse sequence, where the transferred vortex remains trapped within the supersolid, and the angular momentum is sustained over long times.

V. CONCLUSION

In this paper, we have demonstrated that the orbital angular momentum of an LG beam can be coherently transferred to a dipolar BEC via STIRAP, but the extent to which it survives and the associated vortex dynamics it engenders are profoundly governed by the underlying interaction-driven dipolar phase. Our results demonstrate that the combination of long-range dipole-dipole interactions, trap anisotropy, and coherent light-matter coupling enables rich and phase-sensitive vortex dynamics and collective excitation phenomena.

In the superfluid phase, the condensate supports stable vortex excitations whose dynamics are principally determined by external confinement and interaction parameters, with angular momentum well retained over long times. The quantum fluctuations, represented by the

Lee-Huang-Yang correction, stabilize the droplet phase, in which the vortex remains pinned within the density profile but exhibits complex dynamics, accompanied by the fragmentation and subsequent recombination of droplets, leading to only partial retention of angular momentum with oscillations. In the supersolid phase, the spontaneous breaking of continuous translational symmetry introduces density modulation and reduces interdroplet phase coherence, yielding a qualitatively distinct evolution of the vortex compared to both superfluid and droplet phases. Unlike in the droplet, where the vortex remains confined, in the supersolid phase, the reduced superfluid fraction and density modulation cause the vortex to delocalize and eventually leave the condensate, with angular momentum averaging to zero. However, reorienting the magnetic polarization along the beam propagation direction restores angular momentum conservation and stabilizes the vortex within the supersolid, highlighting the crucial role of geometric alignment between the dipole polarization and the LG beam in coherent light engineering. In this regard, the interplay between geometric alignment, trap anisotropy, and vortex stability in the droplet phase opens promising avenues for future exploration.

Further, we examined the role of collective excitations, such as scissors and quadrupole modes, in the population-transferred anisotropic dipolar condensates. These modes are excited by the combined effect of dipolar anisotropy and trap deformation, reflecting the broken rotational symmetry of the system. Their behavior evolves systematically from robust long-lived oscillations in the superfluid to rapid suppression in the supersolid, mirroring the structural evolution of the condensate across the three phases.

Overall, our results establish a versatile and controllable route to engineer vortex states and probe collective excitations in dipolar Bose gases via coherent light-matter coupling, where the underlying dipolar phases play a crucial decisive role in determining the outcome.

This work not only enhances our understanding of vortex nucleation, angular momentum retention, and collective dynamics in dipolar gases but also opens new avenues for coherent-state engineering in strongly correlated systems. The theoretical framework developed here is readily extendable to spin-orbit-coupled Bosonic gases and other strongly correlated dipolar systems, offering promising directions for ongoing and future experiments in ultra-cold quantum matter.

VI. ACKNOWLEDGEMENTS

We acknowledge the National Supercomputing Mission (NSM) for providing computing resources of PARAM Shakti at IIT Kharagpur, which is implemented by C-DAC and supported by the Ministry of Electronics and Information Technology (MeitY) and Department of Science and Technology (DST), Government of India. S.H. acknowledges the MHRD Government of India for the research fellowship. D.S. acknowledges the MHRD Government of India for the research fellowship. H.S.G. and A.S. gratefully acknowledge the support from the Prime Minister's Research Fellowship (PMRF), India. S.M. gratefully acknowledges the financial support from the Science and Engineering Research Board (SERB) MATRICS project under Grant No. MTR/2023/000457.

Appendix A: Equation of Motions

In this section, we provide a detailed derivation of the Raman-coupled extended Gross-Pitaevskii Eq. (3) mentioned in the main text, Sec. II. Let $\hat{\Psi}_i^\dagger$ and $\hat{\Psi}_i$ be the creation and annihilation operators, respectively, for atoms in the state $|i\rangle$. Let us consider that the Hamiltonian \hat{H} for interacting bosons confined in a trapping potential, written in a frame rotating at the frequency of the applied laser fields within the rotating-wave approximation, is given by [6, 53]:

$$\hat{H} = \hat{H}_0 + \hat{H}_c + \hat{H}_{\text{dd}} + \hat{H}_{\text{LM}} + \int d\mathbf{r} \hbar \delta \hat{\Psi}_3^\dagger(\mathbf{r}, t) \hat{\Psi}_3(\mathbf{r}, t).$$

Where $\hat{H}_0 = \int d\mathbf{r} \sum_{i=1}^2 \hat{\Psi}_i^\dagger(\mathbf{r}, t) \hat{h}_i \hat{\Psi}_i(\mathbf{r}, t)$ with $\hat{h}_i = -\hbar^2 \nabla^2 / 2m_i + V_i(\mathbf{r})$. \hat{H}_c and \hat{H}_{dd} are intra- and inter contact and dipole-dipole interaction terms, respectively.

$$\hat{H}_c = \frac{1}{2} \int d\mathbf{r} \sum_{i,j=1}^2 U_{ij} \hat{\Psi}_i^\dagger(\mathbf{r}, t) \hat{\Psi}_j^\dagger(\mathbf{r}, t) \hat{\Psi}_j(\mathbf{r}, t) \hat{\Psi}_i(\mathbf{r}, t)$$

$$\hat{H}_{\text{dd}} = \frac{1}{2} \int d\mathbf{r} \sum_{i,j=1}^2 \int d\mathbf{r}' \hat{\Psi}_i^\dagger(\mathbf{r}, t) \hat{\Psi}_j^\dagger(\mathbf{r}', t) V_{\text{dd}}^{ij}(\mathbf{r} - \mathbf{r}') \hat{\Psi}_j(\mathbf{r}', t) \hat{\Psi}_i(\mathbf{r}, t)$$

The short-range contact intra- and inter-component interaction strengths are denoted by $U_{ii} = 4\pi\hbar^2 a_{ii}/m_{ii}$ and $U_{ij} = 2\pi\hbar^2 a_{ij}/m_{ij}$, respectively. Here a_{ii} and a_{ij} are intra- and inter-species s-wave scattering lengths, and $m_{ij} = m_i m_j / (m_i + m_j)$ is the reduced mass. And $V_{\text{dd}}^{ij}(\mathbf{r} - \mathbf{r}') = C_{\text{dd}}^{ij} (1 - 3 \cos^2 \theta) / 4\pi |\mathbf{r} - \mathbf{r}'|^2$ and $C_{\text{dd}}^{ij} = \mu_0 \mu_i^m \mu_j^m$, where μ_0 is the vacuum permeability and μ_i^m ($i = 1, 2$) is the magnetic moment. \hat{H}_{LM} designates the coupled LM interaction energy between states $|1\rangle$ and $|3\rangle$, and $|3\rangle$ and $|2\rangle$ with the LG laser modes having l_1 and l_2 units of charge, respectively. \hat{H}_{LM} is given as

$$\hat{H}_{\text{LM}} = \int d\mathbf{r} \left(\sum_{i=1}^2 \hbar \Omega_i(\mathbf{r}, t) \hat{\Psi}_3^\dagger(\mathbf{r}, t) \hat{\Psi}_i(\mathbf{r}, t) + \text{h.c.} \right)$$

Here, $\Omega_1(\mathbf{r})$ and $\Omega_2(\mathbf{r})$ are the Rabi frequencies of the transitions $|1\rangle \rightarrow |3\rangle$ and $|3\rangle \rightarrow |2\rangle$, given by: $\Omega_1(\mathbf{r}, t) = \mathbf{E}_1(\mathbf{r}, t) \cdot \mathbf{d}_{13}/\hbar$ and $\Omega_2(\mathbf{r}, t) = \mathbf{E}_2(\mathbf{r}, t) \cdot \mathbf{d}_{32}/\hbar$ where \mathbf{d}_{13} and \mathbf{d}_{32} are the transition dipole moments. We consider $\mathbf{d}_{13} = \mathbf{d}_{23} = \mathbf{d}$. From Eqs. 1 and 2, we obtain

$$\Omega_i(\mathbf{r}, t) = (E_{\text{max}} d / \hbar) r_{\perp}^{|l_i|} \exp\{-i(k_i z - l_i \varphi - \omega_i t)\} \exp\{-r_{\perp}^2 / w_i^2\} \exp\{-(t - \tau_i)^2 / T^2\}.$$

The last term determines light interaction in state $|3\rangle$, where δ is the detuning.

Starting from the bosonic commutation relations

$$\begin{aligned} [\hat{\Psi}_i(\mathbf{r}, t), \hat{\Psi}_j^\dagger(\mathbf{r}', t)] &= \delta(\mathbf{r} - \mathbf{r}') \delta_{ij}, \\ [\hat{\Psi}_i(\mathbf{r}, t), \hat{\Psi}_j(\mathbf{r}', t)] &= 0, \\ [\hat{\Psi}_i^\dagger(\mathbf{r}, t), \hat{\Psi}_j^\dagger(\mathbf{r}', t)] &= 0, \end{aligned}$$

and employing the Heisenberg equation of motion

$$i\hbar \partial_t \hat{\Psi}_i(\mathbf{r}, t) = [\hat{\Psi}_i(\mathbf{r}, t), \hat{H}],$$

We obtain the following dynamical equations:

$$\begin{aligned} i\hbar \partial_t \hat{\Psi}_i(\mathbf{r}, t) &= \left[\hat{h}_i + \sum_{j=1}^2 U_{ij} \hat{\Psi}_j^\dagger(\mathbf{r}, t) \hat{\Psi}_j(\mathbf{r}, t) \right] \hat{\Psi}_i(\mathbf{r}, t) \\ &+ \sum_{j=1}^2 \int d\mathbf{r}' V_{\text{dd}}^{ij}(\mathbf{r} - \mathbf{r}') \hat{\Psi}_j^\dagger(\mathbf{r}', t) \hat{\Psi}_j(\mathbf{r}', t) \hat{\Psi}_i(\mathbf{r}, t) \\ &+ \hbar \Omega_i^*(\mathbf{r}, t) \hat{\Psi}_3(\mathbf{r}, t), \quad i = 1, 2. \end{aligned}$$

$$\begin{aligned} i\hbar \partial_t \hat{\Psi}_3(\mathbf{r}, t) &= \hbar \delta \hat{\Psi}_3(\mathbf{r}, t) + \hbar \Omega_1(\mathbf{r}, t) \hat{\Psi}_1(\mathbf{r}, t) \\ &+ \hbar \Omega_2(\mathbf{r}, t) \hat{\Psi}_2(\mathbf{r}, t) \end{aligned}$$

Assuming the adiabatic elimination condition, i.e, the value of detuning δ is large [6], so the field operator $\hat{\Psi}_3(\mathbf{r}, t)$, i.e. $i\hbar\partial_t\hat{\Psi}_3(\mathbf{r}, t) = 0$, we can create a dark state, which will show zero loss of the particles from the intermediate state. The adiabatic elimination condition builds a relation among the field operators: $\delta\hat{\Psi}_3(\mathbf{r}, t) = -\Omega_1(\mathbf{r}, t)\hat{\Psi}_1(\mathbf{r}, t) - \Omega_2(\mathbf{r}, t)\hat{\Psi}_2(\mathbf{r}, t)$. This relation modifies the dynamical equations of $\hat{\Psi}_1(\mathbf{r}, t)$ and $\hat{\Psi}_2(\mathbf{r}, t)$:

$$\begin{aligned} i\hbar\partial_t\hat{\Psi}_i(\mathbf{r}, t) &= \left[\hat{h}_i + \sum_{j=1}^2 U_{ij}\hat{\Psi}_j^\dagger(\mathbf{r}, t)\hat{\Psi}_j(\mathbf{r}, t) \right] \hat{\Psi}_i(\mathbf{r}, t) \\ &+ \sum_{j=1}^2 \int d\mathbf{r}' V_{\text{dd}}^{ij}(\mathbf{r} - \mathbf{r}') \hat{\Psi}_j^\dagger(\mathbf{r}', t)\hat{\Psi}_j(\mathbf{r}', t)\hat{\Psi}_i(\mathbf{r}, t) \\ &- \frac{\hbar}{\delta} |\Omega_i(\mathbf{r}, t)|^2 \hat{\Psi}_i(\mathbf{r}, t) \\ &- \frac{\hbar}{\delta} \Omega_j(\mathbf{r}, t)\Omega_i^*(\mathbf{r}, t)\hat{\Psi}_{3-i}(\mathbf{r}, t), \quad i = 1, 2. \end{aligned}$$

At zero kelvin temperature and in the low-energy s -wave scattering limit, the bosonic field operator $\hat{\Psi}_i(\mathbf{r}, t)$ can be approximated by a classical complex-valued wavefunction $\Psi_i(\mathbf{r}, t)$ within the mean-field framework, neglecting quantum fluctuations [53].

$$\begin{aligned} i\hbar\partial_t\Psi_i(\mathbf{r}, t) &= \left[\hat{h}_i + \sum_{j=1}^2 U_{ij}\Psi_j^*(\mathbf{r}, t)\Psi_j(\mathbf{r}, t) \right] \Psi_i(\mathbf{r}, t) \\ &+ \sum_{j=1}^2 \int d\mathbf{r}' V_{\text{dd}}^{ij}(\mathbf{r} - \mathbf{r}') \Psi_j^*(\mathbf{r}', t)\Psi_j(\mathbf{r}', t)\Psi_i(\mathbf{r}, t) \\ &- \frac{\hbar}{\delta} |\Omega_i(\mathbf{r}, t)|^2 \Psi_i(\mathbf{r}, t) \\ &- \frac{\hbar}{\delta} \Omega_j(\mathbf{r}, t)\Omega_i^*(\mathbf{r}, t)\Psi_{3-i}(\mathbf{r}, t), \quad i = 1, 2. \end{aligned} \tag{A1}$$

However, a dipolar Bose gas exhibits interaction-driven density-modulated phases, including droplet and supersolid states. The conventional mean-field description alone is insufficient to stabilize these phases against collapse [18, 19, 24] induced by the dipole-dipole interaction. Consequently, the beyond-mean-field Lee-Huang-Yang (LHY) correction becomes essential for stabilizing droplets and supersolid phases. We include the LHY correction term in Eq. (A1), which accounts for the correction in the chemical potential [14, 80–83].

$$\begin{aligned} i\hbar\partial_t\Psi_i(\mathbf{r}, t) &= \left[\hat{h}_i + \sum_{j=1}^2 U_{ij}\Psi_j^*(\mathbf{r}, t)\Psi_j(\mathbf{r}, t) \right] \Psi_i(\mathbf{r}, t) \\ &+ \sum_{j=1}^2 \int d\mathbf{r}' V_{\text{dd}}^{ij}(\mathbf{r} - \mathbf{r}') \Psi_j^*(\mathbf{r}', t)\Psi_j(\mathbf{r}', t)\Psi_i(\mathbf{r}, t) \\ &- \frac{\hbar}{\delta} |\Omega_i(\mathbf{r}, t)|^2 \Psi_i(\mathbf{r}, t) + \Delta\mu_i\Psi_i(\mathbf{r}, t) \\ &- \frac{\hbar}{\delta} \Omega_j(\mathbf{r}, t)\Omega_i^*(\mathbf{r}, t)\Psi_{3-i}(\mathbf{r}, t), \quad i = 1, 2. \end{aligned} \tag{A2}$$

Along with this tight confinement of the condensate in the $z = 0$ plane and equal frequency ($\omega_1 = \omega_2$) of the laser pulses, the Eq. A2 reduces to the Eq. 3.

Appendix B: The Quasi-2D LHY Correction

In this section, we provide a detailed derivation of the quantum fluctuation Eq. (5) mentioned in the main text, Sec. II. Taking two-component dipolar 3D quantum fluctuation (LHY) [14, 80–83] forms to make it quasi-2D,

$$\begin{aligned} \Delta\mu_i &= \frac{m^{3/2}}{3\sqrt{2}\pi^2\hbar^3} \sum_{\pm} \int_0^1 du \\ &Re \left(\left[\tilde{V}_{ii}^{\text{int}}(u) \pm \frac{(-1)^{i-1}\delta\tilde{V}_{ii}^{\text{int}}(u) + 2\tilde{V}_{12}^{\text{int}}(u)^2 n_{3-i}}{\sqrt{\delta^2 + 4\tilde{V}_{12}^{\text{int}}(u)^2 n_1 n_2}} \right] I_{E\pm}^{3/2} \right) \end{aligned} \tag{B1}$$

with $\delta = n_1\tilde{V}_{11}^{\text{int}}(u) - n_2\tilde{V}_{22}^{\text{int}}(u)$, $\tilde{V}_{ij}^{\text{int}}(u) = \tilde{g}_{ij}^c + \tilde{V}_{\text{dd}}^{ij}(u)$, being the Fourier transform of the total interaction potential, $I_{E\pm} = n_1\tilde{V}_{11}^{\text{int}}(u) + n_2\tilde{V}_{22}^{\text{int}}(u) \pm \sqrt{\delta^2 + 4\tilde{V}_{12}^{\text{int}}(u)^2 n_1 n_2}$. To make quasi-2D, we integrate the Eq. B1 along the z -axis assuming $\Psi_i(\mathbf{r}_{\perp}, z) = \Psi_i(\mathbf{r}_{\perp})\Phi_i(z)$, where $\Phi_i(z) = (1/\pi l_z^2)^{1/4} \exp(-z^2/2l_z^2)$, and we get the Eq. 5.

Appendix C: Collective Excitation Modes

The scissors mode provides direct evidence of the explicit breaking of rotational symmetry by the anisotropic trapping potential and DDI interaction. In the present system, the magnetic field is applied along the y -direction, while the LG beam propagates along the z -axis. Under these conditions, angular momentum is no longer conserved and can be exchanged between the dipolar condensate and the external trap. This exchange generates a restoring torque, leading to an oscillatory motion of the condensate identified as the scissors mode [68, 84–88]. The quadrupole mode, on the other hand, corresponds to a collective deformation of the condensate density profile and is strongly influenced by the anisotropic

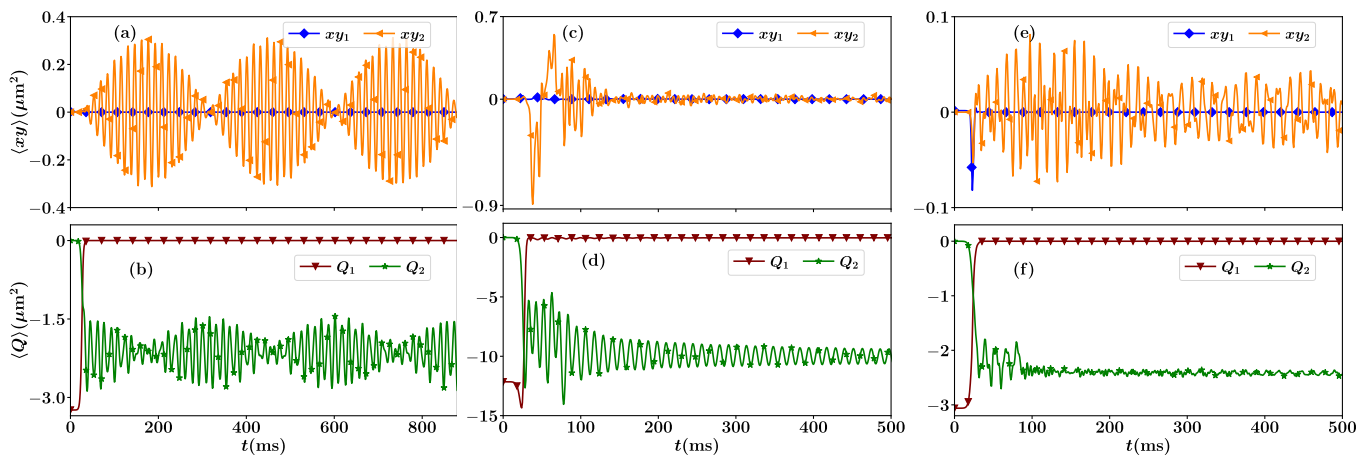


FIG. 7. Time evolution of the scissors $\langle xy \rangle$ and quadrupole $\langle Q \rangle$ modes under the G-LG pulse sequence for the (a,b) superfluid, (c,d) droplet, and (e,f) supersolid phases, respectively. Panels (a,c,e) show the scissors mode, while panels (b,d,f) depict the corresponding quadrupole mode evolution.

dipole-dipole interaction together with the trapping geometry [73, 74].

In the superfluid phase, angular momentum is not conserved, as shown in Fig. 2(c,f). This non-conservation leads to an oscillatory motion of the condensate identified as the scissors mode, as shown in Fig. 7(a). The quadrupole mode is strongly influenced by the anisotropic dipole-dipole interaction together with the trapping geometry, as illustrated in Fig. 7(b). From Figs. 7(a) and 7(b), it is evident that the scissors mode $\langle xy \rangle$, characterized by xy , is coupled to the quadrupole mode $\langle Q \rangle$ associated with the operator $Q = (\omega_x^2/\omega_y^2) x^2 - y^2$.

The angular momentum of light cannot be fully transferred to the droplet or supersolid phases due to the lower superfluid fraction and breaking of rotational symmetry. The angular momentum of these phases of condensates is also not conserved, and its average value is close to $\pm 0.5\hbar$ for the droplet phase, as shown in Fig. 3(c,f). As expected, the condensate undergoes scissors oscil-

lations during the initial phase of dynamics and fades around ≈ 120 ms, as shown in Fig. 7 (c). However, the quadrupole mode persists for a longer duration and remains finite with a gradually decreasing oscillation amplitude up to ≈ 500 ms, as shown in Fig. 7 (d). Compared with the superfluid phase, the oscillation amplitudes are high due to the stronger localization of the droplet state.

For the supersolid phase, the scissors mode remains nearly constant throughout the evolution, as shown in Fig. 7(e), whereas the quadrupole oscillation is prominent only during the initial stage of evolution and becomes strongly suppressed after approximately ≈ 100 ms [see Fig. 7(f)]. Since angular momentum is not conserved [see Fig. 4(c,f)] in the driven Raman-coupled system, the collective excitations exhibit distinct dynamical behavior: the scissors oscillation remains robust over long evolution times, whereas the quadrupole mode is gradually suppressed due to the redistribution of energy among different excitation channels [68–71, 73–75, 87, 89]. These oscillations, therefore, appear as secondary dynamical excitations rather than the primary mechanism governing the long-time evolution.

-
- [1] H. Zeng, W. Zhang, and F. Lin, *Phys. Rev. A* **52**, 2155 (1995).
- [2] B. W. Shore, *Adv. Opt. Photon.* **9**, 563 (2017).
- [3] G. Nandi, R. Walser, and W. P. Schleich, *Phys. Rev. A* **69**, 063606 (2004).
- [4] M. F. Andersen, C. Ryu, P. Cladé, V. Natarajan, A. Vaziri, K. Helmerson, and W. D. Phillips, *Phys. Rev. Lett.* **97**, 170406 (2006).
- [5] H.-R. Chen, K.-Y. Lin, P.-K. Chen, N.-C. Chiu, J.-B. Wang, C.-A. Chen, P. Huang, S.-K. Yip, Y. Kawaguchi, and Y.-J. Lin, *Phys. Rev. Lett.* **121**, 113204 (2018).
- [6] K. Mukherjee, S. Bandyopadhyay, D. Angom, A. M. Martin, and S. Majumder, *Atoms* **9**, 10.3390/atoms9010014 (2021).
- [7] P. K. Mondal, B. Deb, and S. Majumder, *Phys. Rev. A* **89**, 063418 (2014).
- [8] Y. Shin, M. Saba, M. Vengalattore, T. A. Pasquini, C. Sanner, A. E. Leanhardt, M. Prentiss, D. E. Pritchard, and W. Ketterle, *Phys. Rev. Lett.* **93**, 160406 (2004).
- [9] A. L. Fetter and A. A. Svidzinsky, *Journal of Physics: Condensed Matter* **13**, R135–R194 (2001).
- [10] R. Srinivasan, *Pramana* **66**, 3 (2006).
- [11] J. Abo-Shaeer, C. Raman, J. Vogels, and W. Ketterle, *Science (New York, N.Y.)* **292**, 476 (2001).
- [12] S. Das, K. Mukherjee, and S. Majumder, *Phys. Rev. A* **106**, 023306 (2022).

- [13] V. Pastukhov, *Phys. Rev. A* **95**, 023614 (2017).
- [14] R. N. Bisset, L. A. P. n. Ardila, and L. Santos, *Phys. Rev. Lett.* **126**, 025301 (2021).
- [15] E. Casotti, E. Poli, L. Klaus, A. Litvinov, C. Ulm, C. Politi, M. J. Mark, T. Bland, and F. Ferlaino, *Nature* **635**, 327 (2024).
- [16] L. Klaus, T. Bland, E. Poli, C. Politi, G. Lamporesi, E. Casotti, R. N. Bisset, M. J. Mark, and F. Ferlaino, *Nature Physics* **18**, 1453 (2022).
- [17] G. Semeghini, G. Ferioli, L. Masi, C. Mazzinghi, L. Wolswijk, F. Minardi, M. Modugno, G. Modugno, M. Inguscio, and M. Fattori, *Phys. Rev. Lett.* **120**, 235301 (2018).
- [18] A. R. P. Lima and A. Pelster, *Phys. Rev. A* **86**, 063609 (2012).
- [19] A. Boudjemâa, *Journal of Physics B: Atomic, Molecular and Optical Physics* **48**, 035302 (2015).
- [20] Z.-Y. Liu, A.-C. Ji, and Q. Sun, *Phys. Rev. Res.* **6**, 013014 (2024).
- [21] B. Mohamed, H. Ahmed, and M. Atika, *Generalized stability conditions for binary bose mixtures* (2023), arXiv:2308.13608 [quant-ph].
- [22] S. S. Adusumalli, K. Senapati, S. Singh, and A. Khan, *Physics Letters A* **516**, 129638 (2024).
- [23] F. Zhang and L. Yin, *Chinese Physics Letters* **42**, 010302 (2025).
- [24] D. S. Petrov, *Phys. Rev. Lett.* **115**, 155302 (2015).
- [25] X. Liu and J. Zeng, *Chaos, Solitons & Fractals* **160**, 112240 (2022).
- [26] A. Boudjemâa, *Scientific Reports* **11**, 21765 (2021).
- [27] N. M. Hugenholtz and D. Pines, *Phys. Rev.* **116**, 489 (1959).
- [28] S. Halder, K. Mukherjee, S. I. Mistakidis, S. Das, P. G. Kevrekidis, P. K. Panigrahi, S. Majumder, and H. R. Sadeghpour, *Phys. Rev. Res.* **4**, 043124 (2022).
- [29] S. Halder, S. Das, and S. Majumder, *Phys. Rev. A* **109**, 063321 (2024).
- [30] S. Halder, S. Das, and S. Majumder, *Phys. Rev. A* **107**, 063303 (2023).
- [31] H. S. Ghosh, S. Halder, S. Das, and S. Majumder, *Phys. Rev. A* **110**, 033322 (2024).
- [32] S. Sabari, R. Kishor Kumar, and L. Tomio, *Journal of Physics: Conference Series* **2894**, 012015 (2024).
- [33] G. Li, Z. Zhao, X. Jiang, Z. Chen, B. Liu, B. A. Malomed, and Y. Li, *Phys. Rev. Lett.* **133**, 053804 (2024).
- [34] Y. Deng, J. Cheng, H. Jing, C.-P. Sun, and S. Yi, *Phys. Rev. Lett.* **108**, 125301 (2012).
- [35] A. Saboo, S. Halder, M. Thudiyangal, and S. Majumder, *New Journal of Physics* **27**, 043019 (2025).
- [36] A. Alexandrescu, E. Di Fabrizio, and D. Cojoc, *Journal of Optics B: Quantum and Semiclassical Optics* **7**, 87 (2005).
- [37] K. Mukherjee, S. Majumder, P. Mondal, and B. Deb, *Journal of Physics B: Atomic, Molecular and Optical Physics* **51** (2018).
- [38] A. Bhowmik, N. N. Dutta, and S. Majumder, *Phys. Rev. A* **97**, 022511 (2018).
- [39] P. K. Mondal, B. Deb, and S. Majumder, *Phys. Rev. A* **92**, 043603 (2015).
- [40] A. Bhowmik, P. K. Mondal, S. Majumder, and B. Deb, *Phys. Rev. A* **93**, 063852 (2016).
- [41] A. Bhowmik, N. N. Dutta, and S. Das, *The European Physical Journal D* **76**, 139 (2022).
- [42] F. Araoka, T. Verbiest, K. Clays, and A. Persoons, *Phys. Rev. A* **71**, 055401 (2005).
- [43] S. Das, A. Bhowmik, K. Mukherjee, and S. Majumder, *Journal of Physics B: Atomic, Molecular and Optical Physics* **53**, 025302 (2020).
- [44] A. Bhowmik and S. Majumder, *Journal of Physics Communications* **2**, 125001 (2018).
- [45] A. Bhowmik, P. K. Mondal, S. Majumder, and B. Deb, *Journal of Physics B: Atomic, Molecular and Optical Physics* **51**, 135003 (2018).
- [46] K. Mukherjee, S. Majumder, P. K. Mondal, and B. Deb, *Journal of Physics B: Atomic, Molecular and Optical Physics* **51**, 015004 (2017).
- [47] Y. Zhang, X. Su, H. Chen, Y. Hong, J. Li, and L. Wen, *Results in Physics* **54**, 107067 (2023).
- [48] A. Cappellaro, T. Macrì, G. F. Bertacco, and L. Salasnich, *Scientific Reports* **7**, 13358 (2017).
- [49] K.-P. Marzlin, W. Zhang, and E. M. Wright, *Phys. Rev. Lett.* **79**, 4728 (1997).
- [50] A. Saboo, S. Halder, S. Das, and S. Majumder, *Phys. Rev. A* **110**, 033325 (2024).
- [51] M. Lecomte, A. Journeaux, J. Veschambre, J. Dalibard, and R. Lopes, *Phys. Rev. Lett.* **134**, 013402 (2025).
- [52] S. Sabari, R. Kishor Kumar, and L. Tomio, *Phys. Rev. A* **109**, 023313 (2024).
- [53] M. Ghosh Dastidar, S. Das, K. Mukherjee, and S. Majumder, *Physics Letters A* **421**, 127776 (2022).
- [54] R. Nath, P. Pedri, and L. Santos, *Phys. Rev. Lett.* **102**, 050401 (2009).
- [55] M. Raghunandan, C. Mishra, K. Lakomy, P. Pedri, L. Santos, and R. Nath, *Phys. Rev. A* **92**, 013637 (2015).
- [56] P. Shen and K. F. Quader, *Properties of 2d and quasi-2d dipolar bosons with non-zero tilt angles at t=0* (2018), arXiv:1810.03092 [cond-mat.quant-gas].
- [57] P. Pedri and L. Santos, *Phys. Rev. Lett.* **95**, 200404 (2005).
- [58] C. Ticknor, R. M. Wilson, and J. L. Bohn, *Phys. Rev. Lett.* **106**, 065301 (2011).
- [59] M. Klawunn and L. Santos, *Phys. Rev. A* **80**, 013611 (2009).
- [60] U. R. Fischer, *Phys. Rev. A* **73**, 031602(R) (2006).
- [61] J. Crank and P. Nicolson, *Advances in Computational Mathematics* **6**, 207 (1947).
- [62] P. Muruganandam and S. Adhikari, *Computer Physics Communications* **180**, 1888–1912 (2009).
- [63] F. Böttcher, J.-N. Schmidt, M. Wenzel, J. Hertkorn, M. Guo, T. Langen, and T. Pfau, *Phys. Rev. X* **9**, 011051 (2019).
- [64] I. Ferrier-Barbut, H. Kadau, M. Schmitt, M. Wenzel, and T. Pfau, *Phys. Rev. Lett.* **116**, 215301 (2016).
- [65] L. Chomaz, D. Petter, P. Ilzhöfer, G. Natale, A. Trautmann, C. Politi, G. Durastante, R. M. W. van Bijnen, A. Patscheider, M. Sohmen, M. J. Mark, and F. Ferlaino, *Phys. Rev. X* **9**, 021012 (2019).
- [66] L. Tanzi, S. M. Rocuzzo, E. Lucioni, F. Famà, A. Fioretti, C. Gabbanini, G. Modugno, A. Recati, and S. Stringari, *Nature* **574**, 382 (2019).
- [67] K. Mukherjee, T. A. Cardinale, L. Chergui, P. Stürmer, and S. M. Reimann, *The European Physical Journal Special Topics* **232**, 3417 (2023).
- [68] I. Ferrier-Barbut, M. Wenzel, F. Böttcher, T. Langen, M. Isoard, S. Stringari, and T. Pfau, *Phys. Rev. Lett.* **120**, 160402 (2018).
- [69] R. M. W. van Bijnen, N. G. Parker, S. J. J. M. F. Kokkelmans, A. M. Martin, and D. H. J. O'Dell, *Phys. Rev. A* **82**, 033612 (2010).

- [70] S. Giovanazzi, P. Pedri, L. Santos, A. Griesmaier, M. Fattori, T. Koch, J. Stuhler, and T. Pfau, *Phys. Rev. A* **74**, 013621 (2006).
- [71] M. Wenzel, F. Böttcher, T. Langen, I. Ferrier-Barbut, and T. Pfau, *Phys. Rev. A* **96**, 053630 (2017).
- [72] F. Pang, H. He, Y. Zhang, and C. Qu, *Phys. Rev. A* **112**, 033309 (2025).
- [73] H. He, F. Pang, Y. Zhang, and C. Qu, *Phys. Rev. Res.* **7**, 013219 (2025).
- [74] C. Qu, C.-H. Li, Y. P. Chen, and S. Stringari, *Phys. Rev. A* **108**, 053316 (2023).
- [75] K. Kasamatsu, M. Tsubota, and M. Ueda, *Phys. Rev. A* **69**, 043621 (2004).
- [76] S. Halder, H. S. Ghosh, A. Saboo, A. M. Martin, and S. Majumder, *Phys. Rev. A* **111**, 023301 (2025).
- [77] A. Cidrim, F. E. A. dos Santos, E. A. L. Henn, and T. Macrì, *Phys. Rev. A* **98**, 023618 (2018).
- [78] J. M. Escartín, F. Ancilotto, M. Barranco, and M. Pi, *Phys. Rev. B* **105**, 024511 (2022).
- [79] V. Øvereng, A. Baggaley, and L. Angheluta, *Topological interactions in vortex-wave collisions in bose-einstein condensates* (2025), arXiv:2510.01973 [cond-mat.quant-gas].
- [80] J. C. Smith, D. Baillie, and P. B. Blakie, *Phys. Rev. Lett.* **126**, 025302 (2021).
- [81] Y.-C. Zhang, T. Pohl, and F. Maucher, *Phys. Rev. Res.* **6**, 023023 (2024).
- [82] T. Bland, E. Poli, L. A. P. n. Ardila, L. Santos, F. Ferlaino, and R. N. Bisset, *Phys. Rev. A* **106**, 053322 (2022).
- [83] D. Scheiermann, L. A. P. n. Ardila, T. Bland, R. N. Bisset, and L. Santos, *Phys. Rev. A* **107**, L021302 (2023).
- [84] S. M. Rocuzzo, A. Gallemí, A. Recati, and S. Stringari, *Phys. Rev. Lett.* **124**, 045702 (2020).
- [85] I. Ferrier-Barbut, M. Wenzel, F. Böttcher, T. Langen, M. Isoard, S. Stringari, and T. Pfau, *Phys. Rev. Lett.* **120**, 160402 (2018).
- [86] S. Halder, H. S. Ghosh, A. Pelster, and B. P. Venkatesh, *Dynamical probing of superfluidity and shear rigidity in different phases of a dipolar bose-einstein condensate* (2025), arXiv:2512.24108 [cond-mat.quant-gas].
- [87] D. H. J. O'Dell, S. Giovanazzi, and C. Eberlein, *Phys. Rev. Lett.* **92**, 250401 (2004).
- [88] D. Guéry-Odelin and S. Stringari, *Phys. Rev. Lett.* **83**, 4452 (1999).
- [89] L. E. Young-S. and S. K. Adhikari, *Phys. Rev. A* **107**, 053318 (2023).